

LETTER TO THE EDITOR

An accurate measurement of the spectral resolution of the JWST Near Infrared Spectrograph

Anowar J. Shajib^{1,2,3}, Tommaso Treu⁴, Alejandra Melo^{5,6}, Shawn Knabel⁴, Michele Cappellari⁷, and Joshua A. Frieman^{2,3,8}

¹ Center for Astronomy, Space Science and Astrophysics, Independent University, Bangladesh, Dhaka 1229, Bangladesh

² Department of Astronomy & Astrophysics, University of Chicago, Chicago, IL 60637, USA; e-mail: ajshajib@uchicago.edu

³ Kavli Institute for Cosmological Physics, University of Chicago, Chicago, IL 60637, USA

⁴ Department of Physics and Astronomy, University of California, Los Angeles, CA 90095, USA

⁵ Max Planck Institute for Astrophysics, Karl-Schwarzschild-Str. 1, Garching, 85748, Germany

⁶ Technical University of Munich, TUM School of Natural Sciences, Physics Department, James-Franck-Straße 1, 85748 Garching, Germany

⁷ Sub-Department of Astrophysics, Department of Physics, University of Oxford, Denys Wilkinson Building, Keble Road, Oxford, OX1 3RH, UK

⁸ SLAC National Laboratory, 2575 Sand Hill Rd, Menlo Park, CA 94025

Received xxx, xxxx; accepted xxx, xxxx

ABSTRACT

The spectral resolution ($R \equiv \lambda/\Delta\lambda$) of spectroscopic data is crucial information for accurate kinematic measurements. In this letter, we present a robust measurement of the spectral resolution for the JWST's Near Infrared Spectrograph (NIRSpec) in all its modes: fixed slit (FS), integral field spectroscopy (IFS), and multi-object spectroscopy (MOS). We modeled H and He lines of the planetary nebula SMP LMC 58 using a Gaussian line spread function (LSF) to estimate the wavelength-dependent resolution for multiple disperser and filter combinations. We corrected for the intrinsic width of the planetary nebula's H and He lines due to its expansion velocity by measuring it from a higher-resolution X-shooter spectrum. We find that NIRSpec's in-flight spectral resolutions exceed the pre-launch estimates provided in the JWST User Documentation by 5–45% across all the configurations and covered wavelengths. We recover the expected trend that the resolution increases with the wavelength within a configuration. The robust and accurate LSFs presented in this letter will enable high-accuracy kinematic measurements using NIRSpec for applications in cosmology and galaxy evolution.

Key words. Methods: observational – Techniques: spectroscopic – Methods: data analysis

1. Introduction

The JWST's Near Infrared Spectrograph (NIRSpec; Böker et al. 2023) has enabled IR spectroscopy with an unprecedented combination of redshift reach, signal-to-noise ratio, and spatial resolution. One of its key applications is the study of stellar or gas kinematics in distant galaxies (e.g., de Graaff et al. 2024; Xu et al. 2024; Newman et al. 2025), helping us to understand their formation and evolution, the properties of gas outflows, and the impact of black hole and baryonic feedback (D'Eugenio et al. 2024). Furthermore, accurate measurement of the stellar velocity dispersion of lensing galaxies also enables high-precision measurement of the Hubble constant and other cosmological parameters through the method of time-delay cosmography (Shajib et al. 2025; TDCOSMO Collaboration 2025).

Accurate measurement of the line spread function (LSF) or the spectral resolution is a prerequisite to robustly measuring the velocity dispersion σ_* , as the LSF induces additional broadening in the observed lines, which can be parametrized with σ_{inst} assuming a Gaussian LSF. The accuracy requirement on σ_{inst} to achieve a desired level of accuracy on σ_* can be estimated using the relation (Knabel et al. 2025)

$$\frac{\delta\sigma_*}{\sigma_*} \approx \frac{\delta\sigma_{\text{inst}}}{\sigma_{\text{inst}}} \left(\frac{\sigma_{\text{inst}}}{\sigma_*} \right)^2. \quad (1)$$

Therefore, achieving a 1% accuracy in the velocity dispersion, as desirable for precision cosmology (Knabel et al. 2025), requires an estimate of NIRSpec's medium-resolution σ_{inst} accurate to 1.3% and 5.5% for $\sigma_* = 150 \text{ km s}^{-1}$ and 300 km s^{-1} , respectively, for example.

NIRSpec's LSF in the fixed-slit (FS) mode was previously measured from the narrow emission lines of the planetary nebula (PN) SMP LMC 58 (Isobe et al. 2023). These authors find that the resolution is higher by ~10–20% than the pre-launch estimates provided by the JWST User Documentation (JDox).¹ These authors assumed that the intrinsic expansion velocity of the PN is negligible. However, if the true expansion velocity is near the upper limit of typical values (i.e., $\lesssim 30 \text{ km s}^{-1}$; Jacob et al. 2013), its impact may not be non-negligible, especially for the high-resolution grating ($R \sim 2700$), which would require a ~19% correction (~2.7% for medium resolution with $R \sim 1000$). Nidever et al. (2024) find the resolution in the multi-object spectroscopy (MOS) mode's G140H/F100LP configuration to be ~50–85% higher than the JDox estimates, using narrow absorption lines in red giant stars. Through modeling with simulated data in the MOS mode, de Graaff et al. (2024) attribute the discrepancy between direct measurements and JDox estimates to differences in the source morphology. These authors

¹ JDox webpage for NIRSpec dispersers and filters

demonstrate that a point source would lead to ~50-90% higher resolution in the MOS G395H/F290LP configuration than the JDox estimates, which are based on uniformly illuminated slits. However, the predicted resolution by de Graaff et al. (2024) did not account for the additional broadening introduced by the data reduction procedure. Hence, this value is not directly applicable to the reduced data, and a direct measurement from real data remains indispensable. In summary, there is an unfavorably large discrepancy in the estimated resolutions in the literature, and none of them provides an easy-to-use, wavelength-dependent parametrization of the resolution or the LSF's FWHM.

In this letter, we provide a wavelength-dependent parametrization of NIRSpec's resolution for multiple disperser-filter combinations for all of its FS, integral field spectroscopy (IFS), and MOS modes. We measured the resolutions by fitting prominent H and He emission lines for the PN SMP LMC 58 using datasets from JWST calibration programs, which were specifically obtained for wavelength and LSF calibrations. Isobe et al. (2023) also used a subset of this dataset for their LSF measurements. The same PN was also targeted by Jones et al. (2023) to measure the LSF for JWST's Mid-Infrared Instrument (MIRI). Most of the fitted H lines have nearby weaker He multiplets, which are partially or fully blended and need to be accounted for to obtain an accurate characterization of the LSF. As a significant improvement over previous studies, we account for all the blended lines. We simultaneously fit the medium- and high-resolution spectra, thereby allowing lines that are de-blended in the high-resolution spectrum to inform their relative strengths when fitting the medium-resolution one. Furthermore, we corrected for the PN's expansion velocity after directly measuring it from a higher-resolution ($R \sim 6500$) spectrum of the same PN obtained using the Very Large Telescope's (VLT) X-shooter instrument (Vernet et al. 2011).

This letter is organized as follows. In Section 2, we describe the JWST and X-shooter datasets we used. We describe our measurement method and provide the measured values in Section 3, and then conclude the letter in Section 4. Code scripts and notebooks used in this analysis are publicly available on GitHub.²

2. Datasets

We describe the NIRSpec dataset used to measure the spectral resolutions in Section 2.1 and the VLT X-Shooter spectra used to measure the PN's expansion velocity in Section 2.2.

2.1. NIRSpec spectra

To provide instrument calibrations for the NIRSpec, the planetary nebula SMP LMC 58 (also known as IRAS 05248–7007) was observed with two calibration programs. We used data from the program CAL-1125 (PI: J. Muzerolle) for the MOS mode and the program CAL-1492 (PI: T. Beck) for the FS and IFS modes. The FS mode used the S200A1 slit with 0''2 width. We obtained the reduced Level-3 spectra for both programs from the Mikulski Archive for Space Telescopes (MAST) archive, which were reduced with the default JWST pipeline v1.18.0 (Bushouse et al. 2023) with CRDS context `jwst_1364.pmap`.

The FS- and MOS-mode data were already extracted in the form of 1D spectra. For the IFS mode, we summed the spaxels within a circular aperture of radius 0''55, centered on the PN, to obtain the corresponding 1D spectra. The program CAL-1125 obtained the MOS-mode spectra only with the high-resolution

grating. Therefore, we provide the resolution measurement for the MOS mode only in the high-resolution grating.

2.2. VLT X-shooter spectrum

The VLT X-shooter spectrum of the PN was obtained as part of an *Euclid*-preparation program (program ID 110.23Q7.001; *Euclid* Collaboration et al. 2023). The spectrum was obtained with the VIS arm (covering 550–1020 nm) using a 1''2 slit, which has a nominal resolution of $R \sim 6500$.³ We obtained the observed raw dataset from the European Southern Observatory (ESO) Science Portal,⁴ along with the calibration files. We reduced the dataset to produce an extracted 1D spectrum using ESO's X-shooter data reduction pipeline v3.8.1 (Modigliani et al. 2010) with `ESOREFLEX v2.11.5`.

3. Measurement of the NIRSpec resolution

We adopted the Gaussian profile to characterize the NIRSpec LSF. By testing on a single emission line ($\text{Pa}\alpha$) that is not blended with other lines in both high and medium resolutions, we find that the LSF can be well fitted with either a Gaussian or a Voigt profile, with the Voigt profile providing a better fit thanks to one additional degree of freedom. The Lorentzian profile, however, yields a significantly worse fit. We chose the Gaussian profile also because it is ubiquitously used to account for instrumental resolution in measurements of kinematics, for example, with the software program `rPXF` (Cappellari 2017, 2023). The resolution parameter $R \equiv \lambda/\Delta\lambda$ relates to the associated instrumental dispersion σ_{inst} as $R = c/(2.355\sigma_{\text{inst}})$, where c is the speed of light. We parametrize the wavelength dependence of $\sigma_{\text{inst}}(\lambda) = [\sigma'_{\text{inst}}(\lambda)^2 - \sigma_{\text{PN}}^2]^{1/2}$ as

$$\sigma_{\text{inst}}(\lambda) = \left[\left\{ \frac{\sigma'_{\text{piv}}}{1 + \alpha(\lambda - \lambda_{\text{piv}}) / [1 \mu\text{m}]} \right\}^2 - \sigma_{\text{PN}}^2 \right]^{1/2}, \quad (2)$$

where $\sigma'_{\text{inst}}(\lambda)$ is the instrumental dispersion not corrected for the PN's expansion velocity σ_{PN} , σ'_{piv} is the uncorrected instrumental dispersion at the pivot wavelength λ_{piv} , and α is the coefficient in the inverse-linear dependence on wavelength. We chose the inverse-linear λ -dependence for σ'_{inst} because the resolution $R \propto 1/\sigma_{\text{inst}}$ is found approximately linear in λ from the pre-launch estimates, given that $\Delta\lambda$ tends to be approximately constant in wavelength units. We describe our measurement process for $\sigma'_{\text{inst}}(\lambda)$ in Section 3.1 and for σ_{PN} in Section 3.2.

3.1. Emission line fitting from the NIRSpec spectra

We fit the spectra in wavelength slices around several prominent H and He emission lines. The details of the fitted wavelength ranges and the lists of lines within them are provided in Appendix A. Prominent H lines are often accompanied by He lines in close proximity due to the resemblance in their atomic structures. Furthermore, He lines are often multiplets. These lines are partially or fully blended, especially in the medium resolution. For a given combination of mode, disperser, and filter, we simultaneously fit all the lines within the chosen wavelength slices both in the high and medium resolution spectra, while individually constraining σ'_{piv} and α for both gratings. The emission

³ <https://www.eso.org/sci/facilities/paranal/instruments/xshooter/inst.html>

⁴ <https://archive.eso.org/scienceportal/>

² https://github.com/ajshajib/nirspec_resolution

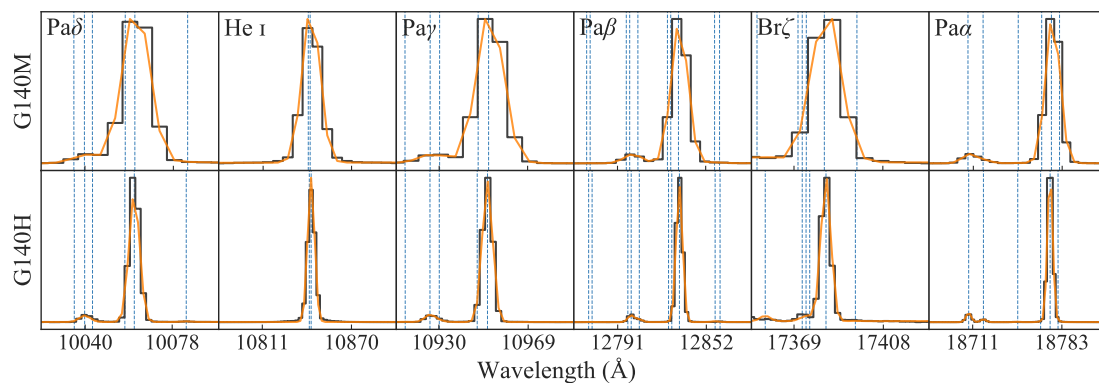


Fig. 1. Post-pixelized Gaussian profile fits (orange) to prominent emission-line groups (black) in the NIRSpec IFS spectra of the PN SMP LMC 58. The IFS-mode G140 disperser is illustrated here as an example among the nine combinations analyzed in this letter. The top row corresponds to the G140M/F100LP configuration (i.e., medium resolution), and the bottom row to G140H/F100LP (i.e., high resolution). The principal line within each group is annotated in the corresponding panel. All the fitted lines in the group are marked with dashed blue lines. The relative amplitudes of all the fitted lines were first obtained in the high-resolution setting, and then the medium-resolution line profiles were fitted with these relative amplitudes fixed. Some lines are clearly separated in the high-resolution case, but partially or fully blended in the medium-resolution one. All of these lines are fitted simultaneously to directly constrain the parameters in $\sigma'_{\text{inst}}(\lambda)$ from Eq. (2).

lines were fitted with post-pixelized Gaussian LSFs. The advantage of fitting all the lines together is that the information from all of them was aggregated to alleviate the issue that the LSF in most configurations is not critically sampled according to the Nyquist sampling theorem. The advantage of fitting both gratings together is that the relative line strengths could first be robustly constrained from the high-resolution spectrum where they are less or not blended, which were then fixed for fitting the blended lines in the medium resolution (see Figure 1). We also fit for the PN’s relative motion v_{PN} (previously measured as $295 \pm 23 \text{ km s}^{-1}$; Reid & Parker 2006) without any dependency on the wavelength. We allowed the PN velocity to be independent between the medium- and high-resolution spectra to account for any residual offset in the wavelength calibration. In each wavelength slice, we fit the continuum level with a linear function. Thus, we have six non-linear parameters in our fitting: σ'_{piv} , α , and v_{PN} for each resolution. The amplitudes of the line profiles and the continuum levels were solved through linear inversion. We obtained the posteriors of the non-linear parameters (provided in Table 1) using the NAUTILUS sampler (Lange 2023).

3.2. Measurement of the PN expansion velocity

To measure the expansion velocity of the PN from the X-shooter spectrum, we require a precise measurement of the spectral resolution of the X-shooter itself. We used the arc-lamp spectrum that was taken for wavelength calibration to obtain a wavelength-dependent estimate of X-shooter’s spectral resolution. We used the PYRIT software program (Prochaska et al. 2020) to measure the FWHMs of the arc-lamp lines in 15 wavelength bins within the covered wavelength range of 550–1020 nm (Figure 2). The uncertainty of the binned measurement was derived from the scatter in the individual-line measurements within each bin. The extent of the variation in the measured resolutions across the wavelength is qualitatively similar to that measured by Gonneau et al. (2020). We fit a quadratic function $R_{\text{xsh}}(\lambda)$ to the measured points. We also simultaneously fit a post-pixelized Gaussian function to the $\text{H}\alpha$ line, which is the most prominent H line within the covered wavelengths. Although a few He lines also fall within the covered wavelength range, they do not significantly add to the constraining power due to their line

Table 1. Best-fit values for parameters in the expression of $\sigma'_{\text{inst}}(\lambda)$ in Eq. (2).

Disperser	Filter	λ_{piv} (Å)	σ'_{piv} (km s $^{-1}$)	α
FS mode				
G140M	F070LP	10111.02	126.08 (05)	0.8313 (45)
G140H	F070LP	10111.02	51.41 (03)	0.4487 (76)
G140M	F100LP	13347.24	96.94 (08)	0.7540 (27)
G140H	F100LP	13347.24	41.62 (03)	0.6857 (31)
G235M	F170LP	22765.89	97.92 (03)	0.5543 (09)
G235H	F170LP	22765.89	39.19 (02)	0.4635 (17)
G395M	F290LP	38474.54	103.62 (07)	0.1872 (21)
G395H	F290LP	38474.54	39.80 (04)	0.1667 (34)
IFS mode				
G140M	F100LP	13539.59	115.80 (02)	0.7622 (04)
G140H	F100LP	13539.59	46.50 (01)	0.8331 (07)
G235M	F170LP	22938.52	110.75 (02)	0.5627 (04)
G235H	F170LP	22938.52	41.70 (03)	0.4988 (17)
G395M	F290LP	38891.71	109.09 (02)	0.2317 (02)
G395H	F290LP	38891.71	41.17 (02)	0.2178 (11)
MOS mode				
G140H	F100LP	13398.32	40.97 (06)	0.6132 (56)
G235H	F170LP	22851.78	41.15 (07)	0.4775 (55)
G395H	F290LP	38621.43	40.48 (14)	0.1594 (62)

Notes. The value of σ_{PN} in Eq. (2) is measured in Section 3.2 to be $\sigma_{\text{PN}} = 6.90 \pm 0.49 \text{ km s}^{-1}$. We do not provide MOS-mode values at medium resolution and the G140/F070LP configuration in IFS mode due to the unavailability of usable data.

strengths being smaller by 1.5 orders of magnitude or more. We parametrized the $\text{H}\alpha$ line’s Gaussian profile with standard deviation $[\sigma_{\text{PN}}^2 + c^2 / \{2.355R_{\text{xsh}}(\lambda_{\text{H}\alpha})\}^2]^{-1/2}$, while allowing the peak position to vary to account for the PN’s relative motion. We constrain the PN’s expansion velocity $\sigma_{\text{PN}} = 6.90 \pm 0.49 \text{ km s}^{-1}$.

We show the measured resolution curves for all the mode–disperser combinations in Figure 3 and compare them to the corresponding pre-launch estimates given by JDox. The resolutions in the IFS mode are ~ 5 – 25% higher than the pre-launch estimates, whereas the resolutions in the FS and MOS modes are ~ 10 – 45% higher.

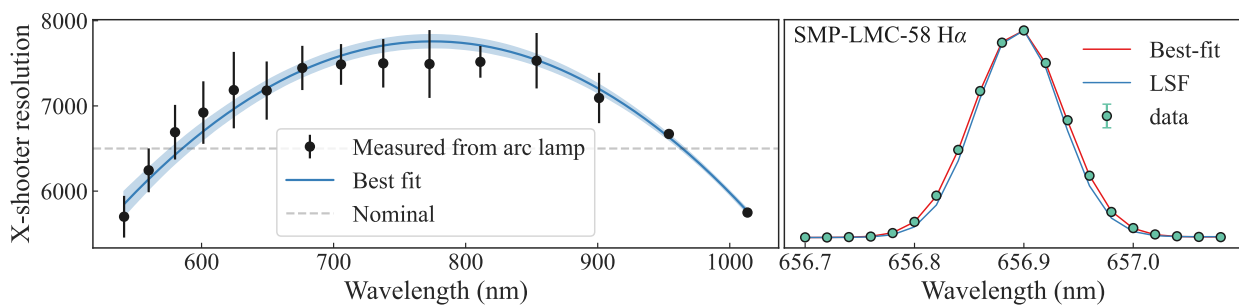


Fig. 2. Measurement of the PN’s expansion velocity. *Left-hand panel:* Measurement of the X-shooter resolution (black points with error bars) from arc-lamp lines with the wavelength dependence modeled with a quadratic function (blue line, with the shaded region showing 1σ uncertainty). *Right-hand panel:* The $H\alpha$ line of the PN in the X-shooter spectra (emerald points). The error bars are too small to be noticeable here. The best-fit post-pixelized Gaussian profile is shown in red, while the width of the X-shooter LSF, as determined by the best fit in the left-hand panel, is shown in blue for comparison. Both sets of illustrated datapoints are simultaneously fit to infer the PN’s expansion velocity $\sigma_{\text{PN}} = 6.90 \pm 0.49 \text{ km s}^{-1}$.

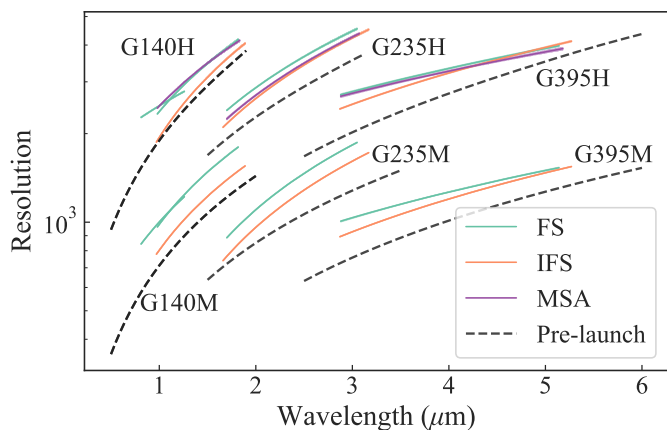


Fig. 3. Comparison of our measured resolution curves in three modes (line colors labeled in the legend) with the pre-launch estimates from JDox (dashed grey lines). The shaded region around each resolution curve signifies the 1σ credible region. The measured resolutions are 5–25% higher than the pre-launch estimates in the IFS mode, and 10–45% higher in the FS and MOS modes.

4. Conclusion

In this letter, we measured NIRSpec’s spectral resolution in multiple configurations for all three of its FS, IFS, and MOS modes. We provide a wavelength-dependent parametrization of the spectral resolution in terms of the instrumental dispersion σ_{inst} by fitting multiple H and He emission lines across the observed wavelength range in the PN SMP LMC 58. We incorporated a correction for the intrinsic width of the PN’s lines, which we measured using a higher-resolution X-shooter spectrum of the same PN.

The measured resolutions increase with wavelength in all configurations, as expected from the pre-launch estimates provided by JDox. For the FS mode, our measured resolution values extend up to 20% higher than those found by Isobe et al. (2023), potentially due to our methodology allowing multiple lines to be fitted within a blended line group.

The parametric wavelength-dependent functions we provide will enable accurate measurements of kinematics from the NIRSpec data, as performed, e.g., by TDCOSMO Collaboration (2025) and Shajib et al. (2025). Although we do not provide the MOS-mode values at the medium resolution, the FS-mode values in medium resolution can be used as a substitute following Isobe et al. (2023), as the slit width for the analyzed data in the FS mode is the same as that of the multi-shutter-array slitlets.

Acknowledgements. We thank Hsiao-Wen Chen, Danial Rangavar Langeroodi, Mark Morris, and Stefan Noll for helpful discussions. This work is based on observations made with the NASA/ESA/CSA James Webb Space Telescope. The data were obtained from the Mikulski Archive for Space Telescopes at the Space Telescope Science Institute, which is operated by the Association of Universities for Research in Astronomy, Inc., under NASA contract NAS 5-03127 for JWST. These observations are associated with programs #1125 and 1492. The specific observations analyzed can be accessed via <https://dx.doi.org/10.17909/m3c0-3t58>. AJS and TT acknowledge support from NASA through STScI grants JWST-GO-2974, HST-GO-16773, and JWST-GO-1974. This research made use of NUMPY (Oliphant 2015), SCIPY (Jones et al. 2001), ASTROPY (Astropy Collaboration 2013, 2018), JUPYTER (Kluyver et al. 2016), MATPLOTLIB (Hunter 2007), SEABORN (Waskom et al. 2014), and NAUTILUS (Lange 2023).

References

- Astropy Collaboration. 2013, A&A, 558, A33
 Astropy Collaboration. 2018, AJ, 156, 123
 Böker, T., Beck, T. L., Birkmann, S. M., et al. 2023, Publications of the Astronomical Society of the Pacific, 135, 038001
 Bushouse, H., Eisenhamer, J., Dencheva, N., et al. 2023, JWST Calibration Pipeline
 Cappellari, M. 2017, MNRAS, 466, 798
 Cappellari, M. 2023, MNRAS, 526, 3273
 de Graaff, A., Rix, H.-W., Carniani, S., et al. 2024, A&A, 684, A87
 D’Eugenio, F., Pérez-González, P. G., Maiolino, R., et al. 2024, Nature Astronomy, 8, 1443
 Euclid Collaboration, Paterson, K., Schirmer, M., et al. 2023, A&A, 674, A172
 Gonneau, A., Lyubenova, M., Lançon, A., et al. 2020, A&A, 634, A133
 Hunter, J. D. 2007, Computing in Science and Engineering, 9, 90
 Isobe, Y., Ouchi, M., Nakajima, K., et al. 2023, ApJ, 956, 139
 Jacob, R., Schönberner, D., & Steffen, M. 2013, A&A, 558, A78
 Jones, E., Oliphant, T., Peterson, P., & Others. 2001, SciPy: Open Source Scientific Tools for Python
 Jones, O. C., Álvarez-Márquez, J., Sloan, G. C., et al. 2023, MNRAS, 523, 2519
 Kluyver, T., Ragan-Kelley, B., Pérez, F., et al. 2016, in Positioning and Power in Academic Publishing: Players, Agents and Agendas, ed. F. Loizides & B. Schmidt (IOS Press BV, Amsterdam, Netherlands), 87–90
 Knabel, S., Mozumdar, P., Shajib, A. J., et al. 2025, TDCOSMO XIX: Measuring Stellar Velocity Dispersion with Sub-Percent Accuracy for Cosmography
 Lange, J. U. 2023, MNRAS, 525, 3181
 Modigliani, A., Goldoni, P., Royer, F., et al. 2010, in Observatory Operations: Strategies, Processes, and Systems III, Vol. 7737, 773728
 Newman, A. B., Gu, M., Belli, S., et al. 2025, arXiv e-prints, arXiv:2503.17478
 Nidever, D. L., Gilbert, K., Tollerud, E., et al. 2024, in IAU Symposium, Vol. 377, Early Disk-Galaxy Formation from JWST to the Milky Way, ed. F. Tabatabaei, B. Barbuy, & Y.-S. Ting, 115–122
 Oliphant, T. E. 2015, Guide to NumPy, 2nd edn. (USA: CreateSpace Independent Publishing Platform)
 Prochaska, J., Hennawi, J., Westfall, K., et al. 2020, JOSS, 5, 2308
 Reid, W. A. & Parker, Q. A. 2006, Monthly Notices of the Royal Astronomical Society, 373, 521
 Shajib, A. J., Treu, T., Suyu, S. H., et al. 2025, arXiv e-prints, arXiv:2506.21665
 TDCOSMO Collaboration. 2025, arXiv e-prints, arXiv:2506.03023
 van Hoof, P. A. M. 2018, Galaxies, 6, 63
 Vernet, J., Dekker, H., D’Odorico, S., et al. 2011, A&A, 536, A105
 Waskom, M., Botvinnik, O., Hobson, P., et al. 2014, Seaborn: V0.5.0 (November 2014)
 Xu, Y., Ouchi, M., Yajima, H., et al. 2024, ApJ, 976, 142

Appendix A: Fitted line lists

In this appendix, we provide the list of fitted lines within the chosen wavelength ranges in Tables A.1, A.2, and A.3 for the G140, G235, and G395 dispersers, respectively. We first obtained a comprehensive list of nebular H and He lines from the Atomic Line List database⁵ (van Hoof 2018). We then aggregated He lines that are close to each other within 1/8th of a pixel size in the corresponding high-resolution spectrum into a single line with an average wavelength weighted by the transition probability (i.e., the Einstein coefficient $g_k A_{ki}$). We adopted 1/8 of the pixel size here, as this is half of the target threshold for wavelength calibration error (Böker et al. 2023). Thus, lines that are separated more closely can be sufficiently considered indistinguishable in the spectrum. Not all the line groups were fitted in some modes, as those line groups fall fully or partially outside of the covered wavelength range in the particular modes. The tables in this appendix specify the modes for which each line group was fitted.

Table A.1. Line list in the fitted wavelength ranges for the G140 disperser.

Principal Line	λ_{\min} (Å)	λ_{\max} (Å)	H lines (Å)	He lines (Å)	Mode
Pa η	8980	9060	9017.385	8999.448, 9002.207, 9011.625, 9013.688	FS (070LP)
Pa ζ	9190	9290	9231.547	9212.861, 9215.757, 9227.763, 9230.392	FS (070LP)
Pa δ	10020	10100	10052.128	10025.946, 10030.471, 10033.901 10048.008, 10074.794	FS, IFS, MOS
He	10780	10900	–	10832.057, 10833.273	FS, IFS
Pa γ	10910	10990	10941.090	10905.195, 10915.994, 10920.055 10936.607	FS, IFS, MOS
Pa β	12760	12885	12821.590	12759.178, 12761.554, 12786.127 12788.433, 12794.005, 12814.100 12816.340, 12846.135, 12849.524	FS (F100LP), IFS, MOS
Br ζ	17350	17430	17366.850	17340.346, 17356.484, 17358.152 17359.750, 17379.672	FS (F100LP), IFS, MOS
Pa α	18675	18820	18756.130	18690.446, 18702.347, 18730.012 18748.470, 18762.520	IFS

Notes. The λ_{\min} and λ_{\max} columns provide the limits of the fitted wavelength ranges. The mode column provides the modes for which the corresponding line group was included in the fit.

⁵ v.300b5: <https://linelist.pa.uky.edu/newpage/>

Table A.2. Line list in the fitted wavelength ranges for the G235 disperser.

Principal Line	λ_{\min} (Å)	λ_{\max} (Å)	H lines (Å)	He lines (Å)	Mode
Br η	16800	16850	16811.111	16801.166, 16802.417, 16804.238 16812.264	IFS
Br ζ	17300	17440	17366.850	17332.122, 17334.426, 17340.346 17356.484, 17358.152, 17359.750 17379.672	FS, IFS, MOS
Pa α	18655	18840	18756.130	18690.446, 18702.347, 18730.012 18748.470, 18762.520	FS, IFS, MOS
He	20555	20660	–	20565.536, 20582.065, 20586.905 20592.793, 20605.478, 20607.440 20622.819	FS, IFS
Br γ	21575	21750	21661.200	21586.002, 21613.713, 21622.911 21633.577, 21647.434, 21652.342 21655.380	FS, IFS, MOS
Br β	26180	26350	26258.670	26192.126, 26205.629, 26240.932 26247.940, 26254.427, 26259.100	FS, IFS, MOS
Pf η	30350	30480	30392.022	30337.982, 30348.429, 30357.263 30373.932, 30378.344, 30379.607 30399.159, 30408.587	IFS, MOS

Notes. The λ_{\min} and λ_{\max} columns provide the limits of the fitted wavelength ranges. The mode column provides the modes for which the corresponding line group was included in the fit.

Table A.3. Line list in the fitted wavelength ranges for the G395 disperser.

Principal Line	λ_{\min} (Å)	λ_{\max} (Å)	H lines (Å)	He lines (Å)	Mode
Pf η	30330	30520	30392.022	30318.738, 30323.249, 30337.982 30348.429, 30357.263, 30373.932 30378.344, 30379.607, 30399.159 30408.587, 30444.836, 30476.839	FS, IFS, MOS
Pf γ	37350	37580	37405.560 37493.933	37328.390, 37344.208, 37381.965 37388.446, 37390.291, 37393.705 37397.995, 37411.662, 37440.355 37442.284, 37450.136, 37473.193 37474.795, 37477.586, 37478.614 37483.145	FS, IFS
Br α	40300	40730	40522.620	40377.329, 40391.224, 40409.405 40490.196, 40506.090, 40512.200 40544.911, 40563.509, 40574.568	FS, IFS
He	42900	43100	–	42954.167, 42959.415	FS, IFS, MOS
Hu ζ	43725	43900	43764.544	43708.509, 43739.438, 43744.948 43746.575	FS, IFS, MOS
Hu δ	51230	51450	51286.570	51195.942, 51212.387, 51214.216 51216.767, 51255.944, 51263.452 51265.485, 51267.336, 51271.545 51273.953, 51341.610	IFS

Notes. The λ_{\min} and λ_{\max} columns provide the limits of the fitted wavelength ranges. The mode column provides the modes for which the corresponding line group was included in the fit.